ELSEVIER

Volume 183, Issue 12, December 2010

JOURNAL OF SOLID STATE CHEMISTRY

www.elsevier.com/locate/jssc

CONTENTS

Abstracted/indexed in BioEngineering Abstracts, Chemical Abstracts, Coal Abstracts, Current Contents/Physics, Chemical, & Earth Sciences, Engineering Index, Research Alert, SCISEARCH, Science Abstracts, and Science Citation Index. Also covered in the abstract and citation database SCOPUS®. Full text available on ScienceDirect®.

Regular Articles

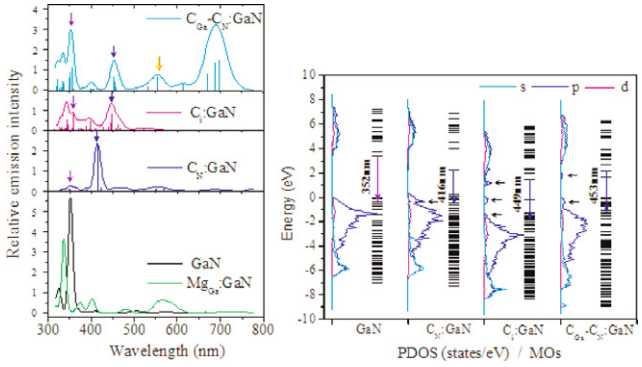

Carbon dopant may introduce the different acceptor or donor level. The blue luminescence of C:GaN are considerable in the region of 400–480 nm, especially that of C_N:GaN.

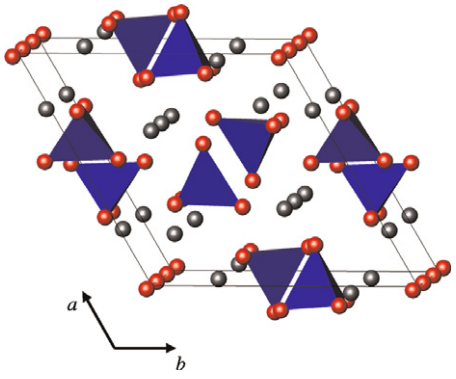

In reactions between the apatites $La_{9.67}Si_5CoO_{26}$ and $La_{10}(Si/Ge)_5CoO_{26.5}$ and NH_3 (g) at temperatures $T > 500\,^{\circ}C$, the partial substitution of the Si and Ge by Co seems to discourage O^{2-}/N^{3-} substitution in favour of the reduction of the metal.

Regular Articles—Continued

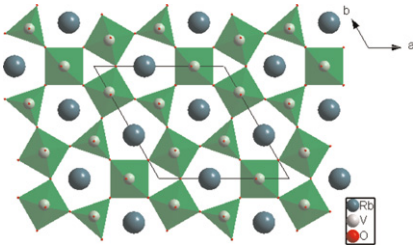

The new nonlinear optical crystal $Rb_3V_5O_{14}$ has been synthesized by solid state reaction and characterized by single-crystal X-ray diffraction, IR and thermogravimetric analysis. The crystal $Rb_3V_5O_{14}$ crystallizes in the trigonal system with space $P31m$ (No. 157), $a = b = 8.7134(12)$ Å, $c = 5.2807(11)$ Å and $\alpha = 90°$, $\beta = 90°$, $\gamma = 120°$, $Z = 1$, $\rho = 3.516$ g/cm^3. It is a layered structure that is very flat and strongly parallel to c. The Kurtz powder SHG measurement, using 1064 nm radiation, showed that the second-harmonic generation efficiency of $Rb_3V_5O_{14}$ is about two times that of KDP.

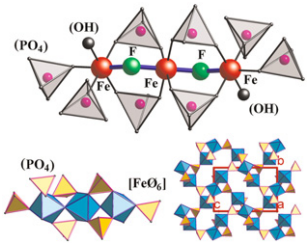

The three-dimensional open-framework structure of $(NH_4)_4Fe_3(OH)_2F_2[H_3(PO_4)_4]$ is built from a novel isolated, linear $(FeO_4)_3(OH)_2F_2$ trimer of corner-sharing Fe(III) octahedra linked by PO_4 tetrahedra.

Continued

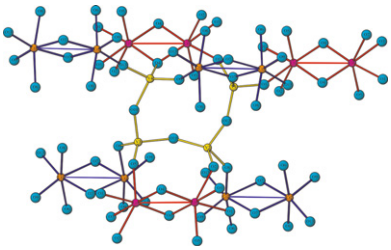

A tetravanadate of chromium ($Cr_2V_4O_{13}$) is prepared characterized in detail. The crystal structure of this compound is formed by the U shaped V_4O_{13} (tetravanadates) and Cr_2O_{10} (dimer) units.

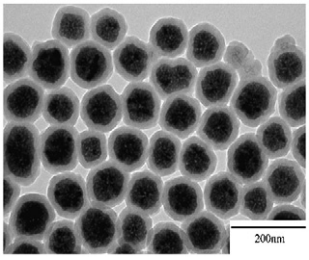

Uniform and monodisperse Gd_2O_3:Eu^{3+} and Gd_2O_3:Eu^{3+}@SiO_2 monodisperse were synthesized by annealed relative parent's $Gd(OH)_3$:Eu^{3+} and $Gd(OH)_3$:Eu^{3+}@SiO_2, respectively. Their morphology and luminescence properties all strongly depended on the iron concentration.

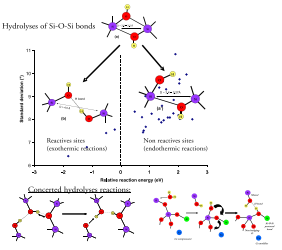

Reactivity within glass bulk: structures obtained after hydrolyses reactions (endothermic and exothermic processes) and mechanisms involving Si–OH, Al–OH, Si–OH–Al groups within aluminosilicates glasses (through ab initio molecular dynamics): formation of the Si–OH–Al entity coupled with an H exchange—Frédéric Bouyer and Grégory Geneste.

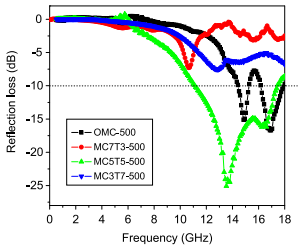

Ordered mesoporous C–TiO_2 nanocomposite with crystalline framework possess excellent microwave absorbing properties with the maximum reflection loss of −25.4 dB and the bandwidth lower than −10 dB is 6.6 GHz.

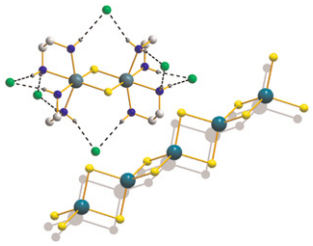

The structure of $[In(en)_2S]_2 \cdot 2Cl$ contains a cationic core and $[Mg(en)_3][In_2S_4]$ is the first thioindate with a charge compensating Mg^{2+} complex. Thermal decomposition yields α- or β-In_2S_3 resp. spinel-type nanocrystalline $MgIn_2S_4$.

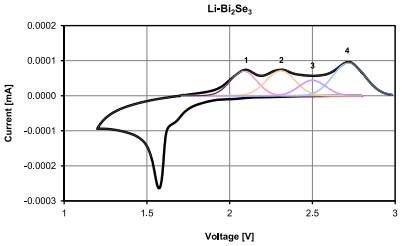

Insertion/extraction of lithium ions into/from Bi_2Se_3 layered crystals was investigated by cyclic voltammetry. The extraction of Li^+ results in the appearance of four bands on the voltammograms. The first two bands have a character of a reversible process. A part of Li^+ ions is bound firmly in the crystal due to the formation of negatively charged clusters of the ($LiBiSe_2.Bi_3Se_4^-$) type. Their extraction needs higher voltage due to the negative charge.

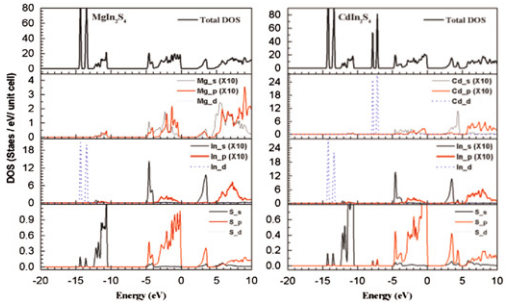

Calculated total and partial densities of states for $MgIn_2S_4$ and $CdIn_2S_4$.

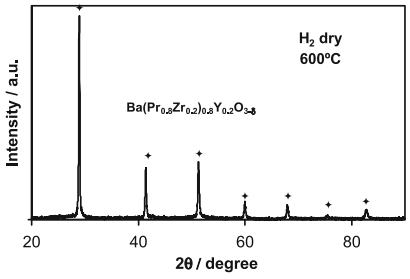

The stability of $Ba(Pr_{1-x}Zr_x)_{0.9}Y_{0.1}O_{3-\delta}$ and $Ba(Pr_{1-x}Zr_x)_{0.8}Y_{0.2}O_{3-\delta}$ systems has been assessed in various atmospheres for $0 \leq x \leq 1$. The figure shows that, by correct compositional selection, stability in reducing conditions can even extend to compositions containing high levels of Pr, such as $Ba(Pr_{0.8}Zr_{0.2})_{0.8}Y_{0.2}O_{3-\delta}$.

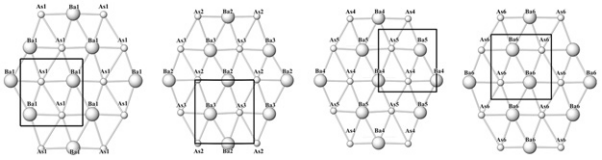

Mesh type and topological structure of the cation layers seen along [0 0 1]; *a*-axis vertical, *b*-axis horizontal. A trace of the unit cell is drawn for reference.

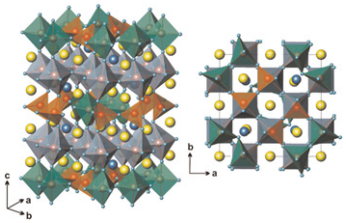

The $Sr_3RFe_4O_{10.5}$ (R = Y, Ho, Dy) anion-deficient perovskites with a complete ordering of the *A*-cations and oxygen vacancies have been prepared using a solid-state reaction in evacuated sealed silica tubes. Oxygen vacancies reside in the $(FeO_{5/4\ 3/4})$ layers, comprising corner-sharing FeO_4 tetrahedra and FeO_5 tetragonal pyramids, which are sandwiched between the layers of the FeO_6 octahedra. Smaller R atoms occupy the 9-fold coordinated position, whereas the 10-fold coordinated positions are occupied by larger Sr atoms.

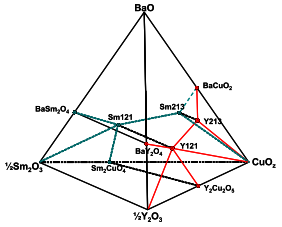

Phase diagram overview of the Ba–Sm–Y–Cu–O system in the BaO-poor region prepared in $p_{O2} = 22$ kPa, 950 °C.

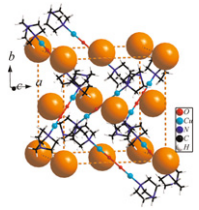

Three new supramolecular compounds based on triethylenediamine and different polyoxometalates have been hydrothermally synthesized and characterized by IR, XPS, TG, elemental analysis and X-ray diffraction analysis.

Continued

Porous α-Fe_2O_3 hollow microspheres and their application for acetone sensor
Shurong Wang, Liwei Wang, Taili Yang, Xianghong Liu, Jun Zhang, Baolin Zhu, Shoumin Zhang, Weiping Huang and Shihua Wu
page 2869

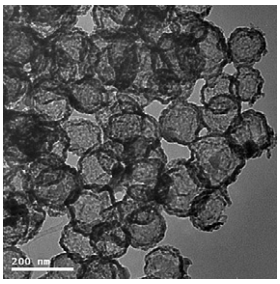

HRTEM images of the α-Fe_2O_3 hollow microspheres.

The intercalation of bicyclic and tricyclic carboxylates into layered double hydroxides
Aamir I. Khan, Gareth R. Williams, Gang Hu, Nicholas H. Rees and Dermot O'Hare
page 2877

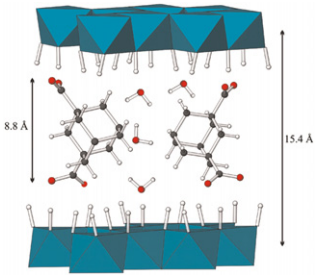

Twenty-four novel nanocomposites built from layered double hydroxides and bicyclic and tricyclic carboxylates have been synthesised and fully characterised. *In situ* X-ray diffraction was used to study reaction mechanisms and kinetics.

Investigation of structural, morphological, luminescent and thermal properties of combusted aluminium-based iron oxide
S.S. Shinde and K.Y. Rajpure
page 2886

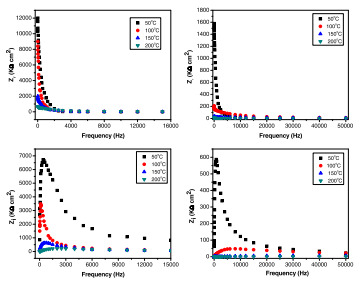

Frequency and temperature dependent interparticle interactions like grains, grain boundary effects using complex impedance spectroscopy of pure and 10 at% Al:Fe_2O_3 have been studied.

***cis-trans* Germanium chains in the intermetallic compounds $ALi_{1-x}In_xGe_2$ and $A_2(Li_{1-x}In_x)_2Ge_3$ (A = Sr, Ba, Eu)—experimental and theoretical studies**
Tae-Soo You and Svilen Bobev
page 2895

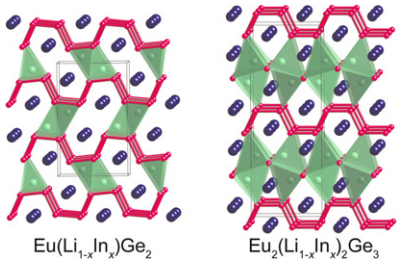

Presented are the single-crystal structures of two types of closely related intermetallics, as well as their band structures, calculated using tight-binding linear muffin-tin orbital (TB–LMTO–ASA) method.

Exchange interaction at the interface of Fe–NiO nanocomposites
S.P. Pati, B. Bhushan and D. Das
page 2903

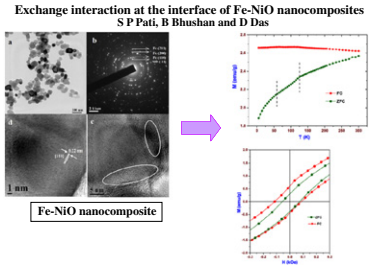

Fe–NiO nanocomposites exhibited some structural disordered region at the interface as revealed by HRTEM. A prominent shift in the hysteresis loops in field cooled condition confirmed the presence of exchange bias at Fe–NiO interfaces. The irreversibility observed in M–T measurements also points to exchange bias effect.

Synthesis, crystal structure, spectrum properties, and electronic structure of a novel non-centrosymmetric borate, $BiCd_3(AlO)_3(BO_3)_4$
Xuean Chen, Hui Yin, Xinan Chang, Hegui Zang and Weiqiang Xiao
page 2910

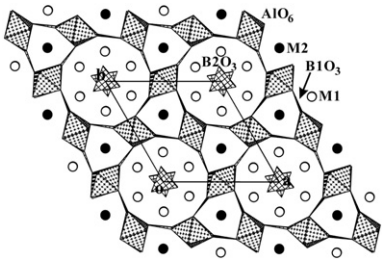

$BiCd_3(AlO)_3(BO_3)_4$ has a 3D network formed by stitching 1D chains of edge-sharing AlO_6 octahedra *via* BO_3 groups. There are channels occupied by Bi^{3+}/Cd^{2+} only or by Bi^{3+}/Cd^{2+} with BO_3 groups.

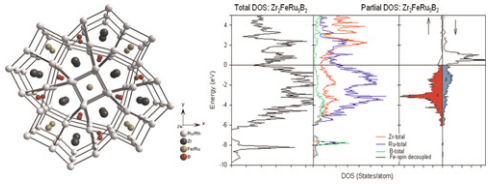

$Zr_2FeRu_{5-x}Rh_xB_2$ ($x = 0$, 1) crystallizes with magnetic atoms forming chains which have been shown to order magnetically depending on the total valence electron count. Magnetic measurements and tight-binding electronic structure calculations are employed to investigate the ordering.

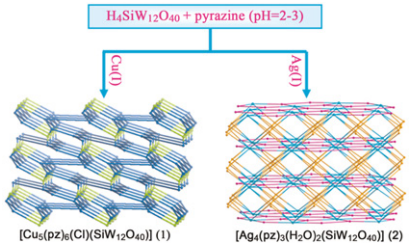

Two new highly connected Keggin POMs-based hybrids have been synthesized by changing metal ions under hydrothermal conditions and the effect of metal ions on the final structure and topology of the POMs-based hybrid compounds was discussed.

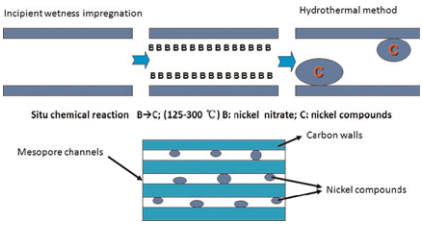

A series of high performance nickel compound/ordered mesoporous carbon composites were synthesized by a combination of incipient wetness impregnation and hydrothermal method for the first time.

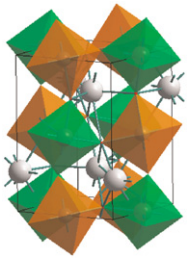

The crystal structures of $Ca_{2-x}La_xFeReO_6$ transform from monoclinic to orthorhombic; meanwhile, high degree of anti-site disorder was present at B/B′ position, which promotes AFM correlations as an La increases.

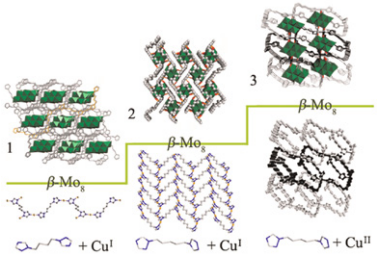

Three 3D compounds based on β-$[Mo_8O_{26}]^{4-}$ clusters with different Cu^I/Cu^{II}-bis(triazole) motifs were synthesized by regularly tuning flexible ligand spacer length and metal coordination preferences.

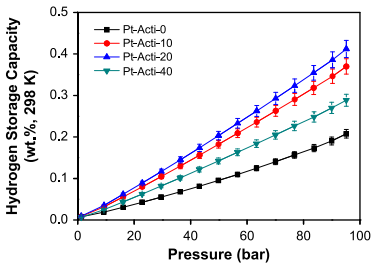

The hydrogen storage capacities of the Pt-loaded activated MWNTs as a function of CO_2 flow time are described.

Continued

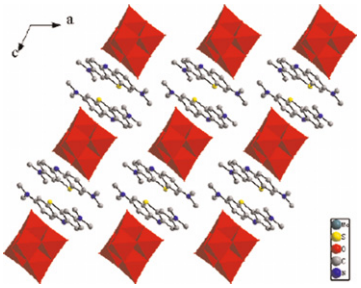

Their crystal structures present that the layers of organic molecules and inorganic anions array alternatively, and there exist strong $\pi\cdots\pi$ stacking interactions between dimeric MB cations.

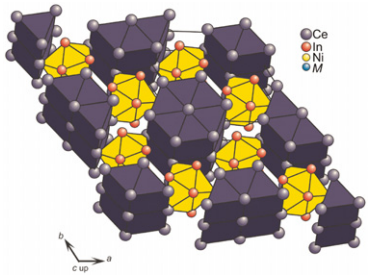

Packing of the polyhedra in the $Ce_7Ni_{4.73}Ge_{3.27}In_6$ structure.

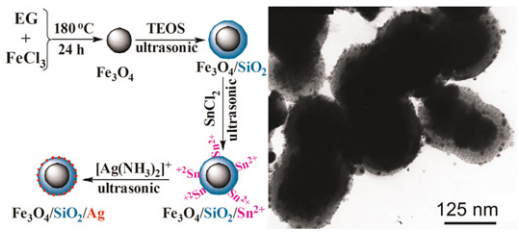

$Fe_3O_4/SiO_2/Ag$ particles, a recyclable surface-enhanced Raman scattering (SERS) material, were designed and synthesized via a simple ultrasonic route.

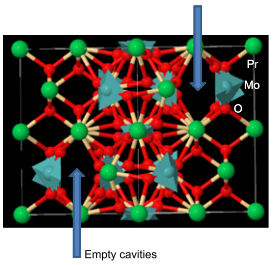

Formerly formulated as Pr_2MoO_6, the title compound is a cubic superstructure of fluorite ($a = 11.0897(1)$ Å, space group *Pn*-3*n*) due to the long-range ordering of PrO_8 scalenohedra and MoO_4 tetrahedral units, showing noticeable shifts of the oxygen positions in order to provide a tetrahedral coordination for Mo ions. A mixed valence Mo^{5+}–Mo^{6+} is identified, which could account for the excellent catalytic properties of this material.

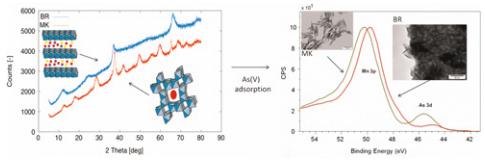

α-MnO_2 (2 × 2 tunnel structure) nanorods and δ-MnO_2 (2-D layered structure) nano-fiber clumps were synthesized in a facile way in an aqueous solution and characterized by TEM, FE-SEM, XRD and BET-N_2 adsorption techniques. The structural analysis shows that α-MnO_2 is needle shaped nanorods and δ-MnO_2 consists of 2-D platelets of fine needle-like fibers arranged in ball-like aggregates. Further batch experiments confirmed that both nanoadsorbents are potential candidates for the adsorption of As(V) with a capacity of 19.41 and 15.33 mg g^{-1} for α-MnO_2 and δ-MnO_2, respectively. The presence of As3*d* peak in XPS study indicates that arsenic on the surface of nanoadsorbents is in the stable form of As(V) with a percentage of arsenate onto α-MnO_2 is 0.099% as compared to 0.021% onto δ-MnO_2, clearly indicating the higher adsorption of As(V) in case of α-MnO_2 as compared to δ-MnO_2, which is in good agreement with the adsorption studies results.

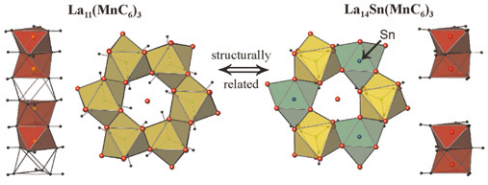

$La_{11}(MnC_6)_3$ with fully ordered superstructure and a new carbide $La_{14}Sn(MnC_6)_3$ were obtained from La/Ni eutectic flux.

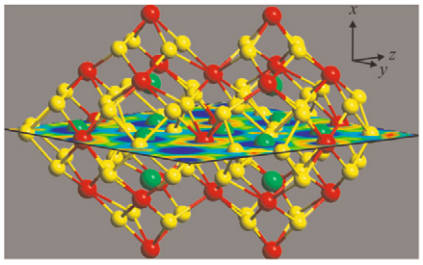

An independent fragment of the 3D [Ag–Mg] framework in $La_4Ag_{10}Mg_3$ together with an ELF section (1/2 0 0 basal plane).

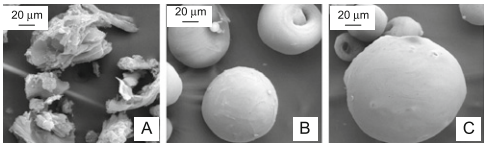

LDHs containing Mg, Al, Fe increase fenbufen solubility, release takes place through ionic exchange with phosphate anions from the medium. Spherical solids with homogeneous, smooth surface are formed when using Eudragit® S 100, efficiently covering the LDH surface.

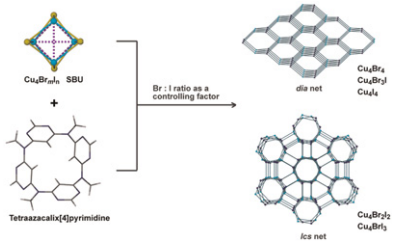

Five luminescent coordination polymers **1**–**5** were obtained via the reaction of tetrahedral $Cu_4Br_{4-m}I_m$ SBUs and a flexible macrocyclic ligand tetraazacalix[4] pyrimidine (TAPM), wherein the Br/I ratio serves as a controlling factor to fine-tune the geometries of $Cu_4Br_{4-m}I_m$ and induce the conformation variation of TAPM, thus constructing two different *dia* and *lcs* topological nets.

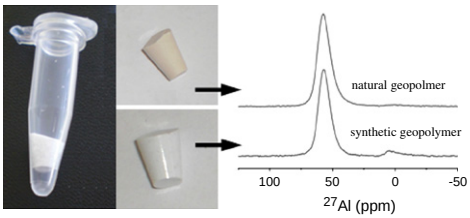

Geopolymer prepared by the sol–gel route has the same spectroscopic properties as the sample prepared from the natural kaolinite.

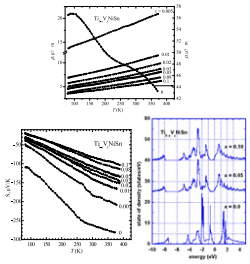

Both approaches experimental and calculations point to the same conclusions. Resisitivity, power factor and thermopower estimations indicate that doping of TiNiSn based compound by the V induces insulator–metal transition without change of the negative sign of *S* thermopower. Vanadium is revealed as donor impurity.

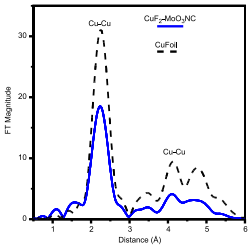

Comparison of Fourier transform of in situ Cu *K*-edge EXAFS spectra for a fully discharged $CuF_2{\bullet}MoO_3$ nanocomposite in a nonaqueous Li cell with that of a Cu foil. Quantitative analysis of the Fourier transforms confirmed that the discharge mechanism for the nanocomposite proceeds via the reaction $CuF_2 + 2Li \rightarrow Cu + 2LiF$. The discharge product of Cu is in the form of highly dispersed nanoparticles.

Continued

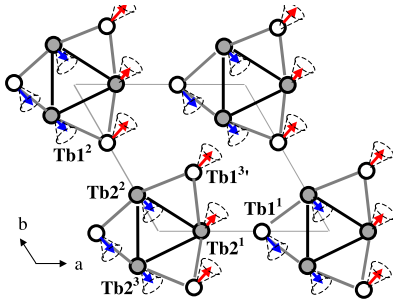

The novel Fe_2P-type $Tb_6\{Fe, Co, Te\}Te_2$ and Er_6FeTe_2 phases (space group $P\bar{6}2m$) show the complex magnetic ordering below 18–228 K. The magnetocaloric effect for Tb_6NiTe_2 in terms of the isothermal entropy change, $-\Delta S_m$, has the maximum value of 4.86 J/kg K at 229 K for the 0–5 T field change.

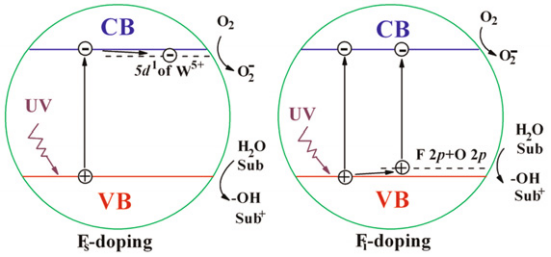

DFT calculations are used to investigate the origin of the improved photo-activity of monoclinic $ZnWO_4$ induced by the substituted and interstitial F-doping. Two possible mechanisms are tentatively put forward according to the F-doping types.

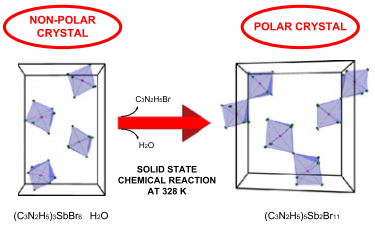

Chemical reaction taking place in $(C_3N_2H_5)_3SbBr_6 \cdot H_2O$ at 328 K.

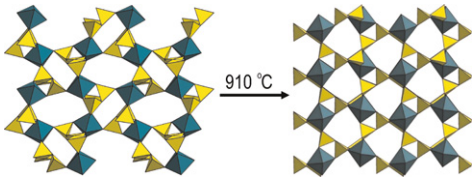

A new microporous zirconosilicate has been prepared by high temperature phase transformation at 910 °C. Its structure has been determined *ab initio* from powder X-ray diffraction data. The water molecules in this material are lost below 125 °C in a way typical of zeolites and molecular sieves.

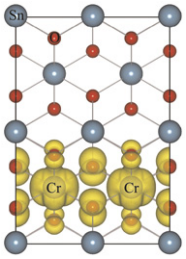

We studied the magnetic properties in Cr-doped SnO_2 by means of the first-principles calculations. It indicated that introduction of oxygen vacancy obviously weakened the ferromagnetic coupling, which could give a rational explanation for the discrepancies in experimental observations.

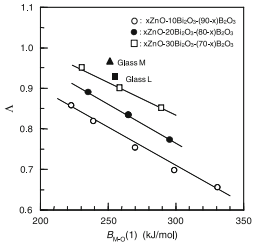

This figure shows the correlation between optical basicity Λ and average single bond strength B_{M-O} in $ZnO–Bi_2O_3–B_2O_3$ glasses. A good correlation is observed, proposing that the average single bond strength is a good parameter for understanding optical properties of $ZnO–Bi_2O_3–B_2O_3$ glasses.

The adsorption of 1,3-butadiene on Pd/Ni multilayers: The interplay between spin polarization and chemisorption strength

Guillermina Gómez, Patricia G. Belelli, Gabriela F. Cabeza and Norberto J. Castellani

page 3086

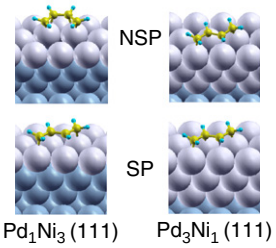

The adsorption of 1,3-butadiene on Pd/Ni(1 1 1) multilayers was theoretically studied. The most stable adsorption site depends on the substrate composition and on the inclusion of spin polarization.

Study of the cation distributions in Eu doped $Sr_2Y_8(SiO_4)_6O_2$ by X-ray diffraction and photoluminescent spectra

Yiqiang Shen, Rui Chen, Fen Xiao, Handong Sun, Alfred Tok and Zhili Dong

page 3093

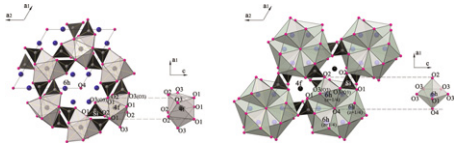

The crystal structures of Eu doped $Sr_2Y_8(SiO_4)_6O_2$ especially the distributions of Eu^{3+} cations between 4*f* and 6*h* sites were studied by X-ray diffraction, Rietveld refinement and photoluminescent spectra.

Rapid Communication

Room temperature ferromagnetism in Mn, Ni and Co ions doped Cu_2O nanorods

Asar Ahmed and Namdeo S. Gajbhiye

page 3100

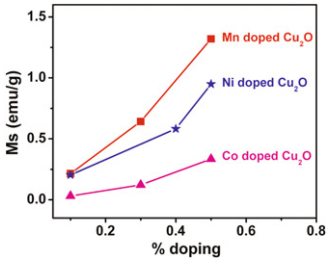

Room temperature ferromagnetism was observed in the Cu_2O nanorods doped with Mn, Ni and Co ions. The origin seems to be the defects of cation vacancies created by the dopant ions.